Simulation of edge localized mode heat pulse using drift-kinetic ions and Boltzmann electrons

I. Joseph[a], M. A. Dorf[a], M. R. Dorr[a]

[a]*Lawrence Livermore National Laboratory, Livermore CA 94551, USA*

Abstract

This article reports on the first dedicated 1D+2V heat pulse propagation studies using the COGENT guiding center kinetic code. The model uses magnetized kinetic ions and a simple Boltzmann electron model. Results agree with previous kinetic and fluid modeling benchmark studies that correspond to the parameters of edge localized modes (ELMs) observed on the JET tokamak. The plasma parameters for the edge pedestal and ensuing ELM dynamics are in the low collisionality regime. Hence, the dominant balance between the assumed Maxwellian ELM source and collisionless parallel advection causes the ion PDF to develop a significantly anisotropic velocity distribution. Adding nonlinear Coulomb ion-ion collisions to the model acts to smooth the sharp features of the ion distribution function, but the anisotropy remains robust due to the low collisionality.

Keywords: kinetic theory, Vlasov equation, magnetic fusion energy, tokamak, edge localized mode
2010 MSC: 00-01, 99-00

1. Introduction

Tokamak fusion reactors are currently envisaged to rely on high performance H-mode operation which suppresses edge turbulence, but comes at the cost of repeated edge localized mode instabilities (ELMs) that deliver heat fluxes that can be large enough to erode target plate and plasma-facing component surfaces. For an H-mode tokamak, the pedestal plasma delivered to the scrape-off layer is typically hot enough to reside in the collisionless regime, where the mean free path is longer than the connection length. In this case, parallel transport along field lines becomes nonlocal and cannot be treated quantitatively with a fluid model. Hence, a large body of recent work [1–8] has focused on understanding the differences between fluid and kinetic models of plasma transport in the tokamak scrape-off layer (SOL) during ELMs. If non-Maxwellian distributions or high-energy tails arise, there can be an enhancement of threshold processes such as radiation, ionization, and sputtering [9]. The nonlinearities involved in the plasma dynamics, materials dynamics, and plasma-materials interactions imply that kinetic effects can be important for making predictions that are accurate enough to be quantitatively compared with experimental results.

In this work, the transient behavior of a plasma heat pulse that travels along a flux tube is studied using the 4D COGENT code [10, 11] in order to predict the heat flux impinging on the target plate of a tokamak divertor. COGENT uses the kinetic guiding center [12] model of magnetized charged particles for ions and has both kinetic and fluid modeling capabilities for electrons. Here, the ions are treated via the drift kinetic equation, while the electrons are treated via a simple Boltzmann model that is similar to the model in Sec. IV C of Ref. [7]. While the effects of kinetic electrons can certainly be important, such effects are outside of the scope of this work. COGENT uses a 2D+2V representation, which is reduced via symmetry to a quasi-1D simulation domain. Hence, these simulations can be considered 1D+2V, where the two velocity space directions are the velocity $v_\parallel$ parallel to the magnetic field $\vec{B}$ and the magnetic moment μ. The results of both collisionless simulations and simulations that use a nonlinear Focker-Planck ion-ion collision operator [13] are compared.

Section 2 describes the model,. Sec. 3 describes the setup for the ELM simulation, and Sec. 4 discusses the results. Finally, conclusions are presented in Sec. 5.

2. Model

In order to obtain a quasi-1D model, the geometry, sources, and initial profiles are assumed to be constant in the radial direction, radially periodic boundary conditions are imposed, and only a small number of grid points are used (see Fig. 1(a) for the spatial grid).

The benchmark case of interest specifies that the magnetic field $\vec{B}$ is constant in magnitude and direction. Hence, the guiding center equations reduce to the drift-kinetic

*Corresponding author: Lawrence Livermore National Lab, Livermore, P.O. Box 808 L-440, Livermore CA 94551, USA. Tel:+1-925-422-3737.
Email address: joseph5@llnl.gov (I. Joseph)

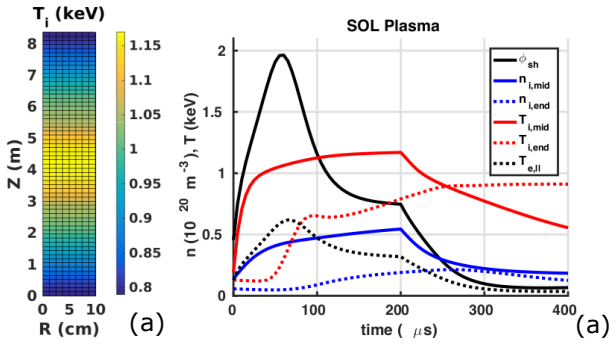

Figure 1: (a) The ion temperature T_i after a 200 μs ELM pulse displayed on the computational grid in configuration space. (b) Plasma properties as a function of time: midpoint $n_{i,mid}$ (blue, solid) and $T_{i,mid}$ (red, solid); end plate $n_{i,end}$ (blue, dotted) and $T_{i,end}$ (red, dotted); $T_{e\|} = \langle T_{i\|} \rangle$ (black, dotted) and ϕ_{sh} (black, solid).

equation:

$$\partial_t f + \vec{\nabla} \cdot \vec{v} f + \partial_{v_\|} Z_i e E_\| f / m_i = S + C[f, f] \qquad (1)$$

where the drift velocity is

$$\vec{v} = v_\| \hat{b} + \vec{E} \times \hat{b} / B, \qquad (2)$$

$C[f, f]$ is the collision operator, and S is a source of particles and energy. Since the electric field $\vec{E}$ only varies in the poloidal direction, the $\vec{E} \times \vec{B}$ drift in the background field generates flow in the radial direction. However, since there is no spatial variation in the radial direction, this radial advection has no impact on the solution.

As in Sec. IV C of Ref. [7], the electrons are treated via an isothermal Boltzmann model. This model assumes that $n_e = n_i$ and that the electric potential ϕ is given by parallel electron force balance

$$e\phi = T_{e\|} \ln (n_i / n_{sh}) + e\phi_{sh} \qquad (3)$$

where the parallel electron temperature $T_{e\|}$ (corresponding to $v_\|$) is constant in space and n_{sh} is the density on the plasma side of the sheath. Following Ref. [7], the parallel electron temperature is assumed to be given by the flux surface average of the parallel ion temperature, $T_{e\|} = \langle T_{i\|} \rangle$. While spatial temperature variation would provide an important correction, the perpendicular size of the SOL is assumed to be much larger than the ion gyroradius, which implies that the more complete gyro-Poisson equation would only produce a small correction to the Boltzmann approximation.

The sheath potential is determined by the electrically insulating (zero current) sheath boundary condition

$$e\phi_{sh} = \tfrac{1}{2} T_{e,sh} \ln \left({v_{i\|}}^2 2\pi / v_{Te,sh}^2 \right) \qquad (4)$$

where $v_{Te,sh} = (T_{e,sh}/m_e)^{1/2}$ and $T_{e,sh}$ is the sheath electron temperature. For the plasma conditions considered here, the electrons are magnetized in the sheath because the ratio of plasma frequency to electron cyclotron frequency is ~ 0.3. Hence, the sheath structure is determined

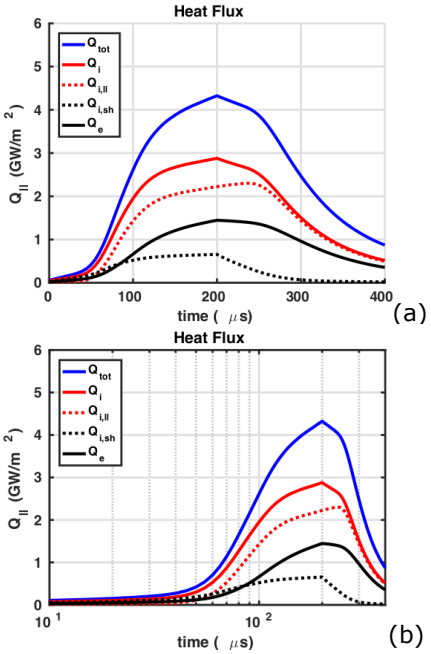

Figure 2: (a) The individual contributions to the heat flux $Q_\|$ vs. time: Q_{tot} (blue, solid), Q_i (red, solid), $Q_{i\|}$ (red, dotted), $Q_{i,sh}$ (black, dotted), Q_e (black, solid); (b) semilog time scale.

by the relation $T_{e,sh} = T_{e\|}$. Since only $E_\|$ is needed for the equations of motion, the sheath parameters are determined via post-processing.

The total heat flux $Q_{tot} = Q_i + Q_e$ parallel to the magnetic field is the sum of the ion and electron components, respectively. The ion heat flux is the sum

$$Q_i = Q_{i\|} + Q_{i,sh}. \qquad (5)$$

The parallel ion heat flux on the plasma side of the sheath is given by

$$Q_{i\|} = \int \left(\tfrac{1}{2} m_i v_\|^2 + \mu B \right) v_\| f_i dv_\| d\mu B. \qquad (6)$$

while the parallel heat flux gained due to ion acceleration through the sheath (essentially transferred from electrons to ions) is given by

$$Q_{i,sh} = Z_i e \phi_{sh} \Gamma_i \qquad (7)$$

where Γ_i is the ion particle flux on the plasma side of the sheath. The parallel heat flux delivered by electrons is

$$Q_e = (T_{e\|} + T_{e\perp}) \Gamma_i. \qquad (8)$$

In the 1D+1V model of Ref. [7], the perpendicular electron temperature in this expression was taken to be the pedestal temperature, T_{ped}, corresponding to the ELM source. In contrast, the 1D+2V model defined here employs the assumption $T_{e\perp} = \langle T_{i\perp} \rangle$, consistent with $T_{e\|} = \langle T_{i\|} \rangle$. Since $T_{i\perp} < T_{ped}$, the effect is to somewhat reduce the electron heat flux.

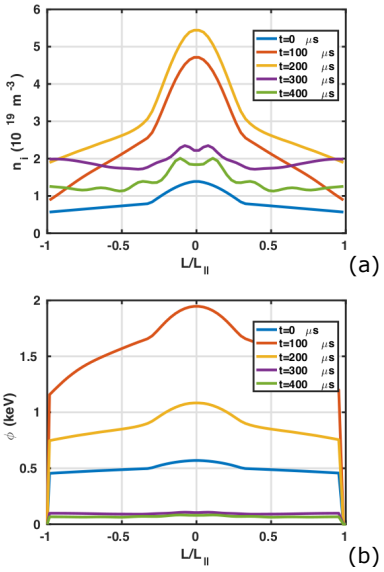

Figure 3: (a) Plasma density n_i and (b) potential ϕ vs. $\ell/L_\parallel$ for various times.

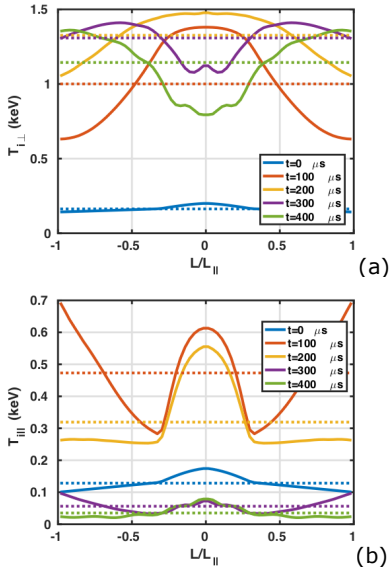

Figure 4: Ion (solid) and electron (dotted) temperature vs. $\ell/L_\parallel$ for various times: (a) $T_\perp$ and (b) $T_\parallel$.

3. Benchmark Case

In accordance with the benchmark cases described in Refs. [1–5, 7, 8], the dimensions of the simulation domain are chosen to qualitatively match the scrape-off layer (SOL) of a "JET-like" tokamak with $R = 3\,\mathrm{m}$ and $B = 3\,\mathrm{T}$. The parallel SOL connection length in the SOL is defined to be $2L_\parallel = 80\,\mathrm{m}$, the field line pitch is constant at 6°, and the nominal SOL width for the ELM-energy release is taken to be $\Delta R = 10\,\mathrm{cm}$. The plasma consists of deuterium ions and the pedestal conditions are assumed to be $n_{ped} = 5 \times 10^{19}\,\mathrm{m}^{-3}$ and $T_{ped} = 1.5\,\mathrm{keV}$. The initial state of the SOL is much cooler and less dense: $n_{SOL} \sim 10^{19}\,\mathrm{m}^{-3}$ and $T_{ped} \sim 150\,\mathrm{eV}$.

The ELM is modeled as a source of particles and energy in the central part of the domain, with a parallel length of $L_{src} = 25\,\mathrm{m}$ and a duration of $\tau_{elm} = 200\ \mu\mathrm{s}$. With the definition $z = 2\ell/L_{src}$, where $z = \ell = 0$ at the midpoint, the source is given by:

$$S(\ell, v_\parallel, \mu) = S_{src} s(z) \frac{e^{-\left(m v_\parallel^2/2 + \mu B\right)/T_{src}}}{(2\pi T_{src}^3)^{1/2}} \tag{9}$$

During the ELM, the temperature is set to correspond to the pedestal $T_{src} = T_{ped} = 1.5\,\mathrm{keV}$ and the magnitude source is set at $S_{src} = 1.2 n_{ped} C_{s,ped}/L_{src} = 9.10 \times 10^{23}\,\mathrm{m}^{-3}$, where the pedestal sound speed is given by $C_{s,ped} = (2T_{ped}/m_i)^{1/2} \simeq 3.79 \times 10^5$ m/s. Before and after the ELM, the source magnitude drops to 1/9 of its value and the source ion temperature is assumed to be 260 eV. The spatial profile of the source $s(z)$ is

$$s(z) = \cos(\pi z/2)\Theta\left(z^2 - 1\right) \tag{10}$$

where Θ is the Heaviside step function.

The total number of particles and the total energy deposited to ions and electrons is given by

$$\Delta N_{elm} = 4 S_{src} H_{src} R \Delta R \tau_{elm} \tag{11}$$
$$\Delta W_{elm} = 3 T_{ped} \Delta N_{elm}. \tag{12}$$

where the poloidal length of the source is $H_{src} = L_{src}\sin(\alpha) = 2.61$ m. For this case, $\Delta N_{elm} = 8.9 \times 10^{20}$ and $\Delta W_{elm} = 0.41$ MJ. For the kinetic ion simulations here, the fluxes arrive on the ion acoustic transit time scale, $\tau_{i\parallel} = L_\parallel/C_{s,ped} = 105\ \mu$s, which is much longer than the electron transit time, $\tau_{e\parallel} = L_\parallel/v_{eT} = 2.5\ \mu$s. If the ELM duration is increased without limit, the particle and heat fluxes will saturate at a constant value determined by the source:

$$\Gamma_{\parallel,sat} = S_{src} L_{src}/\pi \tag{13}$$
$$Q_{\parallel,sat} = 3 T_{src} \Gamma_{\parallel,sat} \tag{14}$$

For this case, $\Gamma_{\parallel,sat} = 7.2 \times 10^{24}\ \mathrm{m}^{-2}$ and $Q_{\parallel,sat} = 5.2\ \mathrm{GWm}^{-2}$. Note that the fluxes normal to the target plates are reduced by the factor $\sin(\alpha) \simeq 0.10$.

The initial conditions are chosen to qualitatively match those described in Refs. [7, 8], which were, in turn, chosen to approximately match the kinetic simulations in Refs. [1–3, 5]. The initial profiles are a shifted Maxwellian with the ion density and temperature corresponding to Ref. [7]:

$$n_i/n_0 = 1 - \delta_{src}|z| + 0.5 s(z) \tag{15}$$
$$T_i/T_0 = 1.45 - 0.45\delta_{src}|z| + 0.3 s(z) \tag{16}$$

where $\delta_s = L_{src}/2L_\parallel = 5/16$, $n_0 = 1 \times 10^{19}\,\mathrm{m}^{-3}$ and $T_0 = 100\,\mathrm{eV}$. In this work, the parallel velocity is chosen to have a linear profile over the source region and constant outflow outside of the source region:

$$v_{i\parallel}/V_1 = z\Theta\left(1 - z^2\right) + \Theta(z-1) - \Theta(-z-1) \tag{17}$$

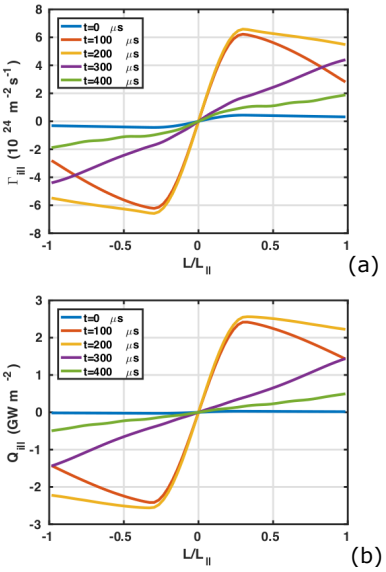

Figure 5: (a) Ion particle flux Γ_i and (b) ion heat flux Q_i vs. $\ell/L_\parallel$ for various times.

where the constant $V_1 = (2T_0/\pi m_i)^{1/2} = 5.52 \times 10^4$ m/s.

In contrast, Ref. [7] initialized with 1/2-Maxwellians that linearly ramp in amplitude across the source region. This leads to a linear ramp in parallel velocity, normalized to the local thermal speed $(2T_i/\pi m_i)^{1/2}$, with purely outgoing distributions beyond the source region.

4. Results

In this section, the results for the benchmark case of an ELM duration of $\tau_{elm} = 200\,\mu$s, corresponding to an ELM energy of 0.41 MW are described in detail. As described in Sec. 3, the strong and hot 1.5 keV pedestal ELM source is applied for $200\,\mu$s. Afterwards, the weaker and colder 260 eV post-ELM source is applied for an additional $200\,\mu$s into the post-ELM period. The simulations are advanced in time with a fourth order Runge-Kutta integrator at a constant time step size chosen to stay near 0.5 of the CFL condition for the advection operator; $\Delta t = 0.5$ μs for 64 poloidal grid points. Due to the fact that the simulations are in the collisionless regime, the CFL condition for the collision operator is less stringent.

The temporal evolution of the density, temperature and sheath potential of a case with $8R \times 64Z \times 64v_\parallel \times 64\mu$ is shown in Fig. 1(b). The upstream profiles (solid) respond strongly to the ELM source and drop sharply after the source is reduced to the post-ELM value. The density and temperature rise from their initial values to values characteristic of the pedestal. It is interesting to note that the downstream temperature increases much more rapidly than the density which may indicate the importance of energetic ions that arrive early. The heat flux Q_{tot}, as well as its various subcomponents Eqs. 8-7, are shown as a function of time in Fig. 2(a,b). The largest subcomponent is

collis-ions	$T_{e\perp}$ model	Q_{pk} (GW/m^2)	$\frac{Q_e}{Q_{pk}}$	W_{tot} (MJ)	$\frac{W_e}{W_{tot}}$	$\frac{W_{pk}}{W_{tot}}$
no	$\langle T_{i\perp}\rangle$	4.32	0.334	0.383	0.335	0.469
no	T_{ped}	4.48	0.357	0.407	0.373	0.474
yes	$\langle T_{i\perp}\rangle$	4.47	0.329	0.393	0.327	0.467
yes	T_{ped}	4.64	0.353	0.418	0.368	0.471

Table 1: Results for peak heat flux Q_{pk}, fraction of electron heat flux Q_e/Q_{pk} at the peak time, total energy W_{tot} delivered over 400 μs, fraction of electron to total energy W_e/W_{tot}, and fraction of energy received before the peak in heat flux to the total W_{pk}/W_{tot}.

from $Q_{i\parallel}$. The spatial profile of various moments at different points in time are shown in Figs. 3-5. Wave-like features can be observed after the ELM source is turned off.

In practice, an accurate determination of the maximum heat flux only requires the velocity space resolution needed for the hot ions. However, capturing the initial distribution, which is 10 times colder, requires good resolution in $v_\parallel$ and μ. A convergence study showed that a resolution of 64×64 in velocity space was sufficient to reduce the convergence error in the heat flux at early times (where the convergence error is largest) to a few percent. The maximum parallel and perpendicular kinetic energies are chosen to be $10T_{ped}$ in order to capture the source relatively well; i.e. the source decreases by $e^{-10} \sim 5 \times 10^{-5}$ along each direction.

The ion particle distribution function (PDF), f_i, is plotted in Fig. 6 at the time of $\tau_{elm} = 200\,\mu$s. Figure 6(a) clearly shows that sonic outflow has developed towards the target plates. Figure 6(b) shows the distribution as a function of $v_\parallel$ and $v_\perp = (2\mu B)^{1/2}$ at the midpoint. The distribution is clearly anisotropic, with $T_{i\parallel} < T_{i\perp}$. If the distribution were isotropic, the contours of f in Fig. 6(b) would lie on semicircles. This anisotropy can also be seen by comparing Figs. 4(a) to 4(b). At the target plate, Fig. 6(c) shows that the distribution consists of almost entirely outgoing $v_\parallel$. While this is to be expected for a collisionless simulation, the PDF at the plate also displays a similar anisotropy as observed at the midplane.

In order to determine the effect of ion-ion collisions, a set of simulations was performed using a nonlinear Fokker-Planck Coulomb collision operator [13]. The spatial profile of the various moments corresponding to Figs. 3-5 are smooth and do not display wave-like structures after the ELM source is turned off. The ion PDF obtained after 200 μs using the collision model is shown in Fig. 7. A comparison of Fig. 6(a,c) with Fig. 7(a,c) demonstrates that collisions provide additional dissipation that tends to smooth the sharp features in phase space. In addition, the relatively sharp structure in Figs. 6(a,b) near the mean flow velocity is broadened. However, the anisotropy in the distribution remains due to the fact that the ELM plasma resides in the collisionless regime.

The source profile and initial conditions are C^0 functions that are not smooth everywhere. This generates

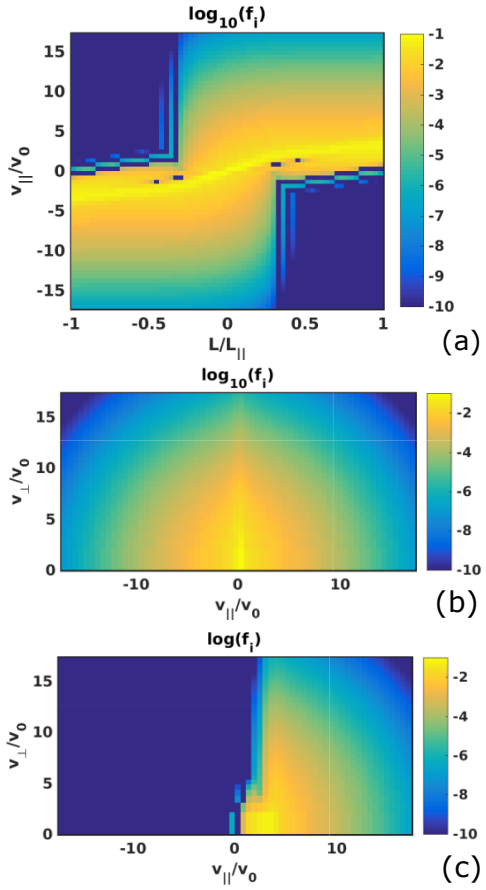

Figure 6: Color plot of $\log_{10}(f)$ for a collisionless simulation at $200\,\mu$s as a function of (a) $\ell/L_\parallel$ and $v_\parallel$ at $\mu = 0$; (b) $v_\parallel$ and $v_\perp = (2\mu B)^{1/2}$ at the midpoint, $\ell = 0$, and (c) same at the target plate, $\ell = L_\parallel$. Note that the distribution is anisotropic, with $T_\parallel < T_\perp = T_{ped} = 1.5\,$keV and transitions to outgoing particles at the target. Velocities are normalized to $V_0 = (100\text{eV}/m_i)^{`/1} = 6.92 \times 10^4$ m/s.

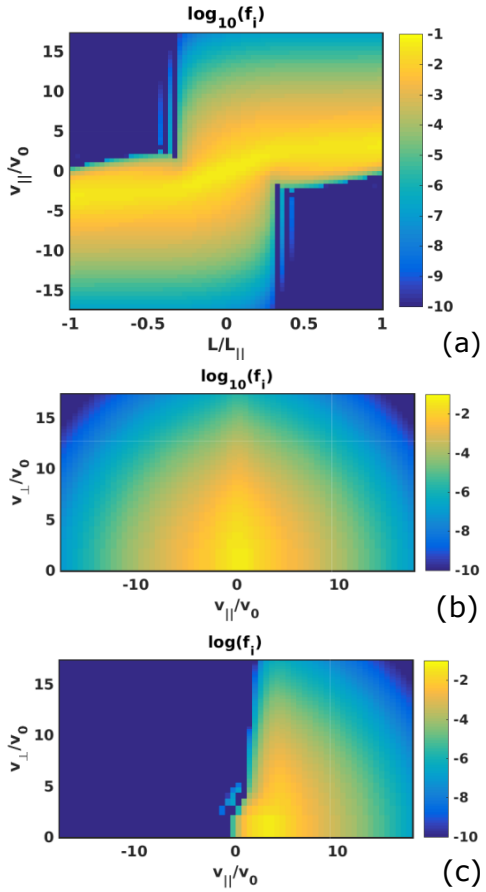

Figure 7: Same as Fig. 6 for a simulation with nonlinear Fokker-Planck ion-ion Coulomb collisions.

sharp features of the PDF that can be observed in Fig. 6-7(a) near the source boundary at $z/L_\parallel = \pm 0.3125$ and in Fig. 6-7(c) near $v_\parallel = 0$. These sharp features cause small numerical artifacts with an amplitude determined by the poloidal spatial resolution and by the choice of numerical advection operator. In the figures, flat shading is used to emphasize these artifacts. While the result for the moments of the distribution, such as the peak heat flux, were little affected by these choices, it was determined that the combination of a 3rd order positivity-preserving upwind advection scheme and a poloidal resolution of 32 or 64 points was sufficient for the purposes here. The use of smoother spatial profiles, such as those used in Ref. [8], reduces the spatial resolution requirements, as does the use of the collision operator, which provides additional dissipation. It would be interesting to study the impact of various choices of numerical advection operators and limiters in the future.

The anisotropy can easily be explained. On timescales longer than the sound transit time, $L_\parallel/C_{s,ped} \sim 105\ \mu$s, parallel advection provides the dominant balance with the source S. Hence, the distribution must approximately satisfy $v_\parallel \partial_\ell f \simeq S$. For zero inflow boundary conditions, this has the solution

$$f(\ell, v_\parallel, \mu) \simeq \int_{-\sigma_v L_\parallel}^{\ell} S(\ell', v_\parallel, \mu) d\ell' / v_\parallel \qquad (18)$$

where $\sigma_v = v_\parallel / |v_\parallel|$. Thus, the PDF is proportional to the source distribution divided by $|v_\parallel|$. A check that the solution satisfies this property at $t = 200\ \mu$s is illustrated in Fig. 8 where a plot of $f|v_\parallel|$ for the collisionless (red) and collisional (blue) cases is compared to a Maxwellian distribution (black) with temperature $T_{ped} = 1.5\,$keV. The $v_\parallel > 0$ (< 0) sides of the figure are taken from the poloidal grid point just ahead (behind) the exact midpoint. The comparison is quite good when the Maxwellian is fitted to f at the maximum $v_\parallel$.

A table of quantities that characterize the collisional and collisionless cases are given in Table 1. The heat flux peaks at 4.32 GW/m^2 for the collisionless simulation and 4.47 GW/m^2 for the simulation with collisions. The heat flux increases until the time that the ELM source is turned off, when it peaks. This is due to the strong dependence of $T_{e\parallel} = \langle T_{i\parallel} \rangle$ on the heating source. The total energy delivered to the target plates over the total 400 μs duration

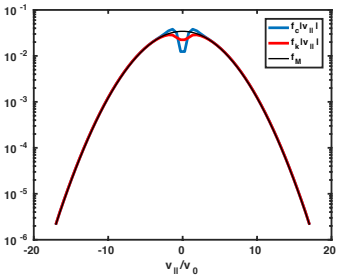

Figure 8: At 200 μs, the ion distribution multiplied by $|v_\parallel|$ is very close to a Maxwellian (labeled f_M, black) with $T = 1.5$ keV; collisional ($f_c|v_\parallel|$ blue), collisionless ($f_k|v_\parallel|$ red).

is $W_{tot} = 0.383$ MW and 0.393 MW, respectively, which is very close to the expected ELM energy. Roughly 1/2 of the energy arrives before the peak in ELM heat flux. The ratio of peak electron to total heat flux and the ratio of electron energy to total energy deposited during the ELM are both close to $\sim 1/3$.

The result for the peak heat flux obtained by assuming $T_{e\perp} = T_{ped}$, 4.48 GW/m^2 compares well to the result reported in E. L. Shi's PhD thesis [14], 4.78 GW/m^2, and lies in between the Vlasov code result 3.92 GW/m^2 and the PIC code result 5.16 GW/m^2 reported in Table 2 of Ref. [5]. For the Boltzmann model, the predicted electron temperature is probably a bit too high relative to the case of kinetic electrons (as can be seen by comparing $T_{i\parallel}$ and $T_{e\parallel}$ in Fig. 4 of Ref. [8]). Thus, the Boltzmann model may overpredict the heat flux relative to Vlasov models with both kinetic electrons and kinetic ions.

5. Conclusions

In conclusion, this article reports on the first results of dedicated studies of 1D+2V "ELM-like" heat pulses using the COGENT guiding center kinetic code. The solutions obtained with kinetic ions and Boltzmann electrons are in quantitative and qualitative agreement with previous kinetic and fluid modeling studies [1–8].

The high pedestal temperature and low density places the dynamics firmly in the collisionless regime. Hence, a balance of the assumed Maxwellian source and collisionless parallel advection causes the ion PDF to develop a significantly anisotropic distribution with $T_{i\parallel} < T_{i\perp}$. The main effect of adding nonlinear ion-ion Coulomb collisions is to smooth the sharp features of the PDF. However, the anisotropy remains robust due to the low collisionality.

The assumption of a Maxwellian source could correspond to a plasma that is predominantly generated by $\vec{E} \times \vec{B}$ transport. Perhaps paradoxically, the equilibrium state generated by a Maxwellian source is singular as $v_\parallel \to 0$. As noted in Ref. [7], particles with $v_\parallel = 0$ will accumulate forever with the pre/post-ELM source specified by the benchmark. Any nominal equilibrium obtained must mollify this singularity in some manner, e.g. via numerical dissipation or physical collisions.

On the other hand, Type-I ELMs are MHD modes and have a strong electromagnetic character at low collisionality. Hence, another possibility is for the transport to be given by the chaotic wandering of magnetic field lines. In the collisionless limit, the effective chaotic diffusion [15] leads to a source of the form $S_m \sim \partial_r D_m \partial_r f$ where the collisionless magnetic diffusion coefficient, $D_{mag} \propto L_\parallel |v_\parallel| (\delta B/B)^2$, is proportional to $|v_\parallel|$. Hence, the assumption of a Maxwellian PDF in the pedestal that diffuses into the SOL via this so-called "magnetic flutter" transport would lead to a source that is precisely $|v_\parallel|$ times a Maxwellian. The results here indicate that such a source would likely lead to an distribution in the SOL that is much closer to Maxwellian.

Future work will study the impact of both kinetic electrons and kinetic ions, with an ultimate view towards evaluation of how plasma-materials interactions are affected by the velocity space distribution.

Acknowledgements

The authors would like to thank E. L. Shi, G. W. Hammett and D. Tskhakaya for helpful discussions and E. L. Shi, in particular, for clarifications on the assumptions within the Boltzmann electron model. This work was performed under the auspices of the US DOE by LLNL under Contract DE-AC52-07NA27344 and is supported by the US DOE Office of Science, Office of Fusion Energy Sciences, and Office of Advanced Scientific Computing Research through the Scientific Discovery through Advanced Computing (SciDAC) project on Plasma-Surface Interactions.

References

[1] R. Pitts, P. Andrew, T. E. G. Arnoux, W. Fundamenski, A. Huber, C. Silva, D. Tskhakaya, J. E. Contributors, Nuclear Fusion 47 (2007) 1437.
[2] D. Tskhakaya, F. Subba, X. Bonnin, D. Coster, W. Fundamenski, R. A. Pitts, J. E. Contributors, Contrib. Plasma Phys. 54 (2008) 022504.
[3] D. Tskhakaya, R. A. Pitts, W. Fundamenski, T. Eich, S. Kuhn, J. E. Contributors, J. Nucl. Mater. 390-391 (2009) 335.
[4] G. Manfredi, S. Hirstoaga, S. Devaux, Plasma Phys. Control. Fusion 53 (2011) 015012.
[5] E. Havlíckovâ, W. Fundamenski, D. Tskhakaya, G. Manfredi, D. Moulton, Plasma Phys. Control. Fusion 54 (2012) 045002.
[6] T. D. Rognlien, R. Cohen, D. D. Ryutov, M. V. Umansky, J. Nucl. Mater. 438 (2013) S418.
[7] E. L. Shi, A. H. Hakim, G. Hammett, Phys. Plasmas 22 (2015) 022504.
[8] Q. Pan, D. Told, F. Jenko, Phys. Plasmas 23 (2016) 102302.
[9] O. Batischev, S. I. Krasheninnikov, P. J. Catto, et al., Phys. Plasmas 4 (1997) 1672.
[10] M. Dorf, M. Dorr, Contrib. Plasma Phys.
[11] M. Dorf, M. Dorr, J. Hittinger, W. Lee, D. Ghosh, J. Comp. Phys. 373 (2018) 446.
[12] J. R. Cary, A. J. Brizard, Rev. Mod. Phys. 81 (2009) 691.
[13] M. A. Dorf, R. H. Cohen, M. Dorr, J. Hittinger, T. D. Rognlien, Cont. Plasma Phys. 54 (2014) 517.
[14] E. L. Shi, Ph.D. thesis, Princeton University (2017).
[15] M. N. Rosenbluth, R. Z. Sagdeev, J. B. Taylor, G. M. Zaslavski, Nucl. Fusion 6 (1966) 297.